Design and Performance Analysis of a Picosecond Pulse Generator

Aaron D. Pitcher, *Graduate Student Member, IEEE*, Charl W. Baard, and Natalia K. Nikolova, *Fellow, IEEE*

***Abstract*— A picosecond pulse generator is designed to generate a stable differentiated Gaussian (monocycle) waveform. The design approach to increasing the center frequency, bandwidth, and peak-to-peak voltage, compared to previously reported ultrawideband (UWB) generators, is described. The 280-ps wide pulse achieves a 1:10 fractional bandwidth (FBW) ratio extending from 500 MHz to beyond 5 GHz at the −10-dB level. A measurement procedure is proposed for evaluating the jitter and noise performance of UWB pulse generators, and it is applied to the fabricated prototype. The procedure exploits jitter and noise definitions from high-speed digital electronics, which are adapted here for the jitter and noise evaluation of UWB pulse generators at microwave frequencies. The problems in obtaining the absolute and relative jitter of a UWB generator are discussed along with proposed solutions. The impact of the input trigger on the pulse stability is demonstrated through the dramatic improvement achieved by the integration of a jitter cleaner in the generator's circuit.**

***Index Terms*— Jitter, measurement techniques, microwave circuits, microwave generation, radar, ultrawideband (UWB).**

I. INTRODUCTION

ULTRAWIDEBAND (UWB) technology is growing at an unprecedented rate due to the development of new sensing and imaging systems. These systems operate in various frequency bands from 100 MHz to 10.6 GHz designated by the Federal Communications Commission (FCC) [1] and other spectrum management bodies [2], [3]. Applications in ground penetrating radar (GPR) and nondestructive testing (NDT) [4]–[6], security and surveillance [6]–[8], and microwave imaging [9]–[11] favor this technology due to its harmless non-ionizing radiation and low-power emissions spread over wide bandwidths. The broad bandwidth provides many advantages over traditional narrowband systems, such as frequency diversity, spread spectrum, improved spatial resolution, penetration depth, and relatively high peak power [12]. The generation of a clean and stable pulse that accurately represents the desired waveform continues to be a major challenge in designing these UWB systems.

A common approach to the generation of an UWB signal is to use a train of Gaussian-like (and higher order Gaussian derivative) waveforms produced by analog discrete circuits [6]–[8], [13]–[21] or complementary metal-oxide-semiconductor (CMOS) integrated circuits (ICs) [22]–[24]. The design requirements involve pulse shaping characteristics, such as full-width at half-maximum (FWHM) pulsewidth, frequency range and bandwidth, peak-to-peak voltage, peak power, and late-time ringing. The CMOS designs provide low power consumption and a single-chip compact form factor but are limited by low output power and relatively narrow bandwidths [17]. The discrete analog designs perform pulse manipulation on an input rectangular or sinusoidal trigger to achieve the desired broadband waveform. They use a combination of avalanche transistors, tunnel diodes, step recovery diodes (SRDs), and linear or nonlinear transmission lines (NLTLs) [12]. They can provide large peak-to-peak voltages and picosecond pulse widths, but they occupy large surface areas and consume significantly more power. The most common design for Gaussian pulse generation uses SRDs, which provides a compromise between the large breakdown voltage and slow switching of the avalanche transistor, and the small breakdown voltage and fast switching of the tunnel diode.

Here, we propose an SRD-based picosecond UWB pulse generator that produces a differentiated Gaussian (monocycle) waveform with a 1:10 fractional bandwidth (FBW) ratio within the low-GHz spectrum. It incorporates a jitter cleaner to remove jitter due to the input trigger. The design builds upon circuits reported in [7], [8], and [13]–[15]. Critical design steps are discussed, which enable significant bandwidth increase without compromising the peak output power and the peak-to-peak voltage. Strategies are also discussed to tune the pulse bandwidth and shape along with the respective limitations.

In addition to the new pulse-generator design, this work offers two main contributions. First, a systematic investigation is carried out regarding the limitations of the design concerning FBW, the upper and lower frequency limits, FWHM pulse width, the peak-to-peak voltage, and the late-time ringing. Second, a rigorous methodology is developed for the noise and the jitter analysis of a UWB pulse generator, which is applied to evaluate the proposed design. Both investigations are based on a statistical evaluation of the generator's performance using thousands of captured waveforms. The proposed methodology for evaluating the jitter and noise performance of the UWB generator exploits definitions from high-speed digital electronics, originally developed for periodic signals in digital clocks and data buses [25]–[27]. We discuss the challenges

---

Manuscript received 22 April 2022; revised 23 June 2022; accepted 9 July 2022. Date of publication 2 August 2022; date of current version 22 November 2022. This work was supported in part by the Defence and Security Accelerator (DASA) Program (Ministry of Defence, U.K.) under Grant DSTLX1000147682 and in part by the Science for Peace and Security (SPS) Program [North Atlantic Treaty Organization (NATO)] under Grant G4992. The Associate Editor coordinating the review process was Dr. Ziqiang Cui. *(Corresponding author: Aaron D. Pitcher.)*

The authors are with the Electromagnetic Vision (EMVi) Research Laboratory, Department of Electrical and Computer Engineering, McMaster University, Hamilton, ON L8S4L8, Canada (e-mail: pitchea@mcmaster.ca).

Digital Object Identifier 10.1109/TIM.2022.3195265

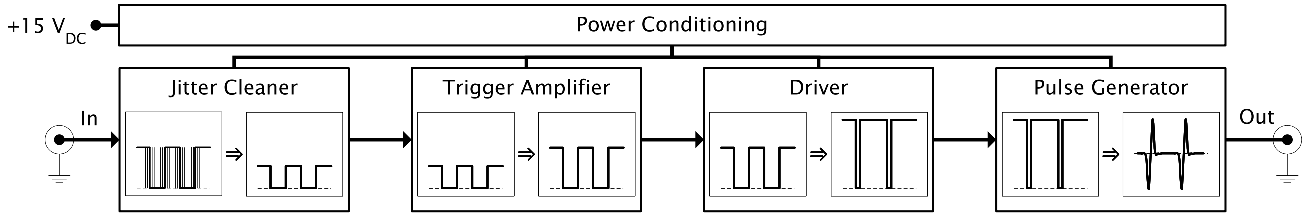

Fig. 1. Block diagram of the picosecond pulse generator.

associated with adapting these definitions and the respective measurement strategies to the case of UWB generators at microwave frequencies.

This article is organized as follows. In Section II, we describe the proposed pulse generator design along with the key tuning strategies. The UWB pulse performance metrics are introduced in Section III along with the respective performance analysis of the proposed generator. We formulate the jitter and noise performance metrics in Section IV and apply them to evaluate the jitter and noise performance of the generator. The results are discussed in Section V followed by conclusions in Section VI.

II. PICOSECOND PULSE GENERATOR DESIGN

The proposed design is based on circuits reported in [7], [8], and [13]–[15]. The principles of operation are briefly described, followed by a discussion of the critical design steps toward larger bandwidth and peak-to-peak voltage along with the key tuning parameters.

A. Design Principles

As shown in Fig. 1, the picosecond pulse generator consists of five major sections: 1) jitter cleaner; 2) trigger amplifier; 3) driver circuit; 4) pulse generator circuit; and 5) power conditioning circuit. Figs. 2–5 show the circuit schematics of the generator's sections. The respective component values are listed in Table I.

1) Jitter Cleaner: The performance and stability of the pulse generator are dependent on the input trigger. The jitter cleaner is critically important to the pulse stability in terms of the pulse repetition interval (PRI) or, inversely, the pulse repetition frequency (PRF). This circuit is shown in Fig. 2 along with the trigger amplifier. The employed jitter cleaner [28] performs jitter attenuation for any transistor-transistor logic (TTL) square-wave input trigger (0-V low, 5-V high) to produce a stable trigger source. Ultralow root-mean-square (rms) output jitter values are expected in the range of 300–400 fs [28]. The IC incorporates a dual-loop phase-locked loop (PLL) that integrates digital signal processing (DSP) circuitry and an ultralow phase noise voltage-controlled oscillator (VCO) [29]. The IC is pin-controlled to set the PRF and PLL bandwidth to phase-lock onto a 1–20-MHz signal. R1 and C1 are chosen to present the input as a 50-Ω load. C2 is an input direct current (dc) block. X1 is a high-quality 114.285-MHz crystal clock.

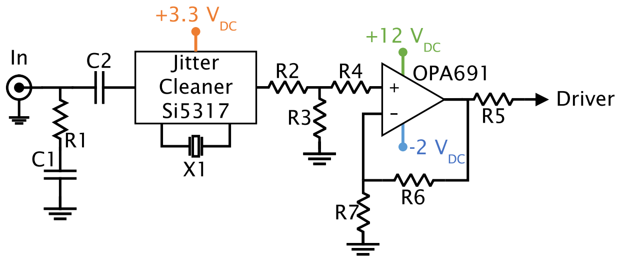

Fig. 2. Jitter cleaner and trigger amplifier circuit schematic.

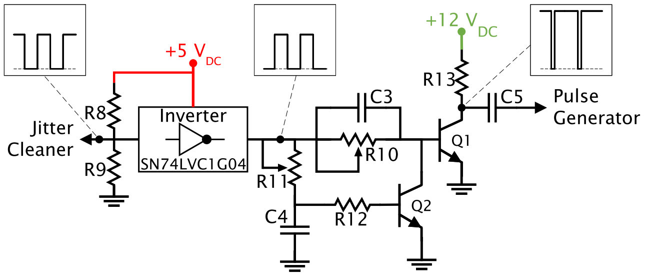

Fig. 3. Driver circuit schematic.

2) Trigger Amplifier: The trigger amplifier translates the output square wave from the jitter cleaner back to the 5-V TTL-level signal. The operational amplifier [30] is dc coupled and designed for a 50-Ω source and a 50-Ω load. The noninverting closed-loop gain is set to 7.6 to yield the correct voltage at the input of the driver circuit. It is important to select a wideband operational amplifier with a sufficient slew rate (SR) to meet the output voltage swing and frequency demands. A minimum SR of 628.3-V/μs is required for a 5-V, 20-MHz square-wave signal.[1]

3) Driver Circuit: The driver circuit (see Fig. 3) accepts the square-wave trigger from the jitter cleaner and the operational amplifier circuit. The inverter [31] inverts the input ensuring constant rise and fall times. The subsequent circuit amplifies the trigger pulse while reducing its duty cycle and increasing the falling-edge's slope. The *RC* integrator (R11 and C4) is responsible for delaying the switching of Q2 with respect to Q1, which reduces the trigger's duty cycle. The delay is controlled by the integrator's time constant as determined by R11 and C4. As described in [14], R13 limits the bias current of Q1, which is switched OFF (nonconducting) in the absence of a trigger pulse. The trigger leads to the discharge

---

[1] A slew rate (SR) was chosen using $SR \geq 2\pi f V/10^6$ [V/μs], where f is the desired PRF in Hz and V is the desired voltage swing in volts.

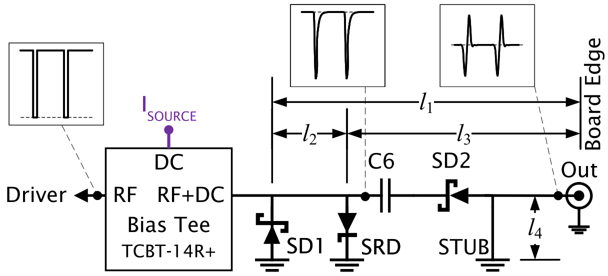

Fig. 4. Pulse generator circuit schematic.

of C3, thus accelerating the switching of Q1 to an ON-state (conducting). At this instant, Q2 is still in an OFF-state until the trigger passes through the RC integrator. At this point, Q2 is switched ON, whereas the base of Q1 is shorted to ground, thus switching Q1 OFF. As the trigger falls to 0-V, Q1 and Q2 return to their original OFF-states until the next trigger arrives. R10 and R12 limit the output current from the inverter to the base of Q1 and Q2. C5 is an output dc block.

4) Pulse-Generator Circuit: The pulse-generator circuit produces the monocycle pulse from the reduced-duty-cycle trigger at the output of the driver circuit. It is shown in Fig. 4. The circuit consists of two pulse-forming networks: 1) SRD-based falling edge sharpener and 2) monocycle forming network [14].

The SRD-based falling edge sharpener consists of a bias tee [32] for the Schottky diode (SD), SD1, and for the SRD. C6 is a dc blocking capacitor needed to forward-bias the SRD (low impedance) and reverse-bias the SD1 (high impedance). The role of the falling edge sharpener is to further reduce the duty cycle by using the SRD as a charge-controlled rapid switch [33]. The SRD is forward-biased so that the trigger switches the diode from forward conduction to reverse cutoff. As the stored charge within the SRD is removed, the diode remains open for a brief moment before it snaps off. The SRD briefly produces a reverse current at the moment of switching as the stored charge dissipates, producing the Gaussian-like pulse. This pulse then propagates in both directions down the coplanar waveguide (CPW) transmission line. As the waveform travels back toward the driver circuit, SD1 switches from reverse bias to forward bias presenting a short circuit. This wave is then inverted and reflected back toward the output SD, SD2. This second SD traps subsequent internal reflections while allowing through only the initial Gaussian-like pulse produced by the SRD. The delay line of length l_2, which lies between SD1 and SRD, plays a crucial role in further sharpening the Gaussian pulse [8]. The distances l_1 and l_3 indicate the SD1 and SRD diode positions in the prototypes, and their difference is the respective l_2 length.

The Gaussian pulse is then submitted to the monocycle forming network, i.e., to the junction with the shorted stub (STUB in Fig. 4). Here, it splits so that one part passes onto the output directly, whereas the other part enters the shorted stub and forms an inverted time-delayed version of the original Gaussian pulse. The direct and reflected portions superimpose to form the monocycle waveform.

TABLE I
PULSE GENERATOR COMPONENTS

Component	Type	Value	Part
R1-3, R5*	Discrete	49.9 Ω	–
R4	Discrete	10 Ω	–
R6†	Discrete	205 Ω	–
R7†	Discrete	33 Ω	–
R8, R9	Discrete	100 Ω	–
R10	Potentiometer	0 – 1 kΩ	3313J-1-102E [34]
R11	Potentiometer	0 – 20 kΩ	3313J-1-203E [34]
R12	Discrete	1 kΩ	–
R13	Discrete	150 Ω	–
R14	Potentiometer	0 – 20 Ω	3313J-1-200E [34]
R15	Discrete	2 Ω	–
R16‡	Discrete	49.9 kΩ	–
C1	Discrete	10 nF	–
C2	Discrete	100 nF	–
C3	Discrete	47 pF	–
C4	Discrete	10 pF	–
C5	Discrete	1 nF	–
C6§	Discrete	5.1 pF	–
Q1, Q2	Transistor	–	BFP196W [35]
SD1, SD2	Discrete	–	BAT15-03W [36]
SRD	Discrete	–	MMD830-0805-2 [37]

* The closest E96 standard resistor value to 50 Ω, which is needed for impedance matching.
† Following [30], R6 and R7 are chosen based on the closest E96 standard resistor to achieve the closed-loop gain of 7.6.
‡ The closest E96 resistor chosen based on recommendations in [38].
§ E24 standard capacitance value.

5) Power Conditioning Circuit: The power conditioning circuit is presented as a block diagram in Fig. 5. It is designed to supply the necessary dc voltage rails (+12, +5, +3.3, and -2 V_{dc}) and one current source to the generator's components. The circuit utilizes dc/dc converters [39], [40] to reduce power dissipation along with low-noise low-dropouts (LDOs) linear regulators [41], [42] to regulate the $+15$-V_{dc} input supply. Low-noise LDOs are chosen to reduce the supply noise on the microwave circuitry. A power-monitoring IC [43] is added to measure the power consumption.

The 200-mA programmable current source [38] supplies the current, I_{SOURCE}, to the pulse-generator circuit. The current supply value is a critical tuning parameter (discussed later), and this tuning is achieved with the R14 potentiometer.

B. Fabricated Prototype

The picosecond pulse generator is fabricated on a four-layer, 1.622-mm (63.9-mil) thick PCB. Annotated photographs of the PCB's top and bottom are shown in Fig. 6. The PCB stackup (as shown in Fig. 7) contains a 0.813-mm (32.0-mil) thick high-frequency RO4003C [44] substrate core stacked on two layers of FR-4 pre-preg and cores. The high-frequency substrate contains all radio frequency (RF) signal paths backed by a ground plane since it has a low dielectric loss, unlike FR-4. The FR-4 layers supply the RF components with power and control paths. The CPW transmission lines (of 50-Ω

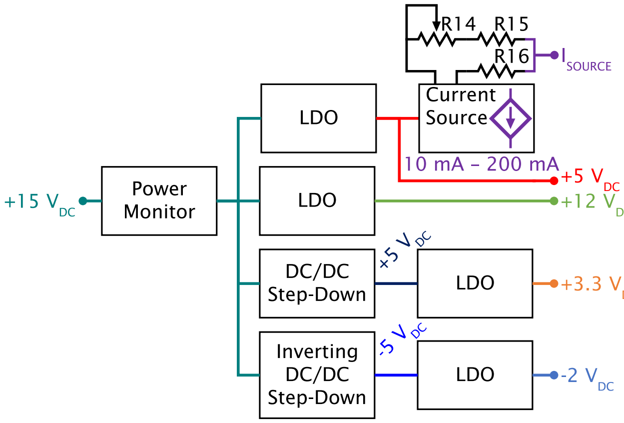

Fig. 5. Power conditioning block diagram. LDO stands for the low-dropout linear regulator.

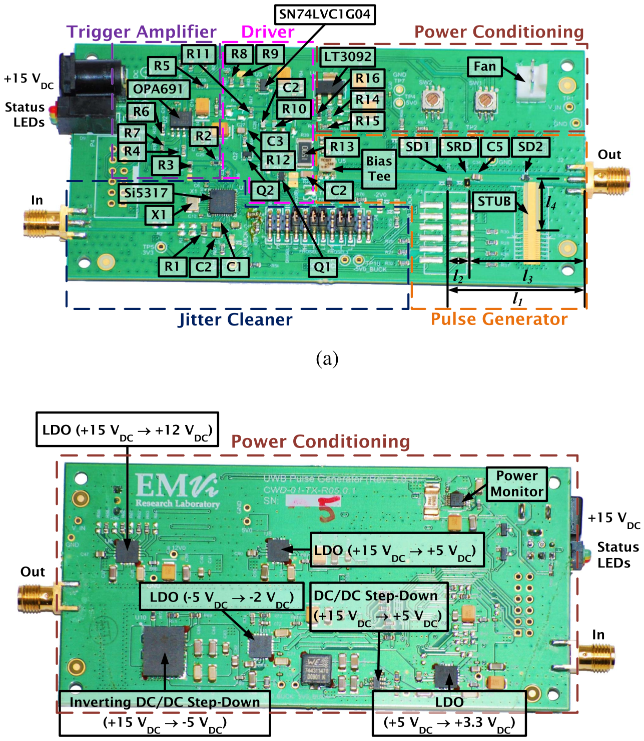

(b)

Fig. 6. Manufactured printed circuit board (PCB) board: (a) top and (b) bottom.

characteristic impedance) are used because they allow for easy shunt-element mounting and the tuning of the shorted stub.

C. Design Tuning and Critical Components

The critical components that lead to significant improvement over the previously reported designs [7], [8], [13]–[15] with the realization of the 1:10 FBW ratio are: 1) high-quality UWB on-chip bias tee; 2) fast-switching wideband negative–positive–negative (NPN) transistors; 3) optimizing the length l_2 between SD1 and SRD; 4) optimizing the length l_4 of the stub; and 5) tuning of the current source supply. The significance of these components is discussed next, along with the tuning strategies.

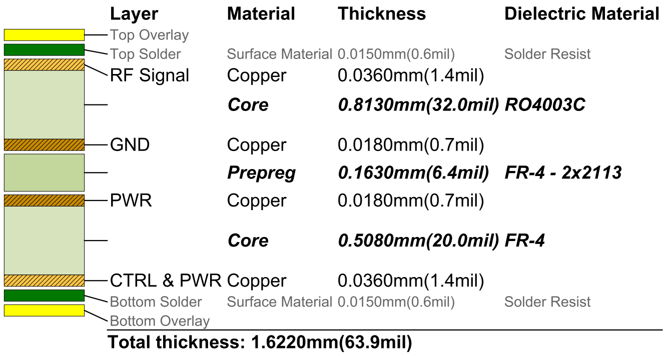

Layer	Material	Thickness	Dielectric Material
Top Overlay			
Top Solder	Surface Material	0.0150mm(0.6mil)	Solder Resist
RF Signal	Copper	0.0360mm(1.4mil)	
	Core	***0.8130mm(32.0mil)***	***RO4003C***
GND	Copper	0.0180mm(0.7mil)	
	Prepreg	***0.1630mm(6.4mil)***	***FR-4 - 2x2113***
PWR	Copper	0.0180mm(0.7mil)	
	Core	***0.5080mm(20.0mil)***	***FR-4***
CTRL & PWR	Copper	0.0360mm(1.4mil)	
Bottom Solder	Surface Material	0.0150mm(0.6mil)	Solder Resist
Bottom Overlay			

Total thickness: 1.6220mm(63.9mil)

Fig. 7. PCB stackup.

TABLE II

DISCRETE COMPONENT REPLACEMENTS FOR POTENTIOMETERS BASED ON MEASURED RESISTANCE OF TUNED GENERATOR

Component	Type	Value	Part
R10	Discrete	249 Ω	–
R11	Discrete	15 kΩ	–
R14	Discrete	12 Ω	–

1) On-Chip Bias Tee: In [7] and [13]–[15], the bias tee to the pulse-generator circuits uses discrete components. Through [8] and this work, it has been found that, despite careful component selection, a bias tee based on discrete components adversely affects the UWB performance of the generator due to insufficient decoupling between the RF and dc signal paths. A commercially available on-chip bias tee [32] has been selected as a replacement, and it has been found to provide lower insertion loss and higher port isolation in the desired bandwidth and well beyond 5 GHz [8].

2) Choice of RF Transistors: The choice of RF transistors for the driver circuit (Q1 and Q2) is also critical. To ensure that the transition of the square wave is sharp, the transition frequency of the transistor must be greater than that of the maximum frequency expected in the picosecond pulse spectrum. Here, this frequency is 5 GHz. In addition, the collector-emitter voltage ratings must meet the 12-V_{dc} supply. A suitable component is the RF NPN bipolar junction transistor (BJT) [35], which is used in the fabricated prototypes. R13 limits its collector current (see Fig. 3), and its resistance is based on the maximum collector current for the device. Note that R13 must be sized to handle the power dissipation. The resistors R10 and R11 have been tuned by hand, and their optimal setting is shown in Table II. The driver is also tuned to achieve the shortest duty cycle with a square waveform shape extending from 0 to 12 V.

3) Length Between SD1 and SRD: The placement of SD1 and SRD in relation to each other plays a critical role in the FWHM pulsewidth of the Gaussian pulse. Several prototypes have been developed [8] with values of the length l_2 from 4 to 10 mm in 2-mm increments. The position of the SRD is kept constant, while SD1 is shifted. As l_2 decreases, the temporal pulsewidth also decreases. Thus, the best performance is achieved at 4 mm [8]. Distances below 4 mm have not been investigated because the physical mounting of the diodes becomes problematic.

4) Stub Length: The tuning of the stub length impacts the higher frequency components of the picosecond pulse. Its tuning results in an impressive increase in the upper frequency limit within the 3–5 GHz with little to no tradeoffs at the lower frequency end. In [14], the stub is viewed as a series capacitance in an *RC* differentiator, where the resistance is the 50-Ω output load. However, this model is valid for a relatively narrow frequency band. In our case, with an FBW ratio on the order of 1:10, the stub can be better represented by a transmission-line model. At the stub junction, about half the incident pulse proceeds directly toward the output port, whereas the other half travels down the stub's shorted end. The shorted end reverses the pulse polarity upon reflection. The pulse in the stub travels two times its length l_4, resulting in a time delay with respect to the incident pulse. The waveform is a superposition of the direct pulse and the inverse-polarity reflected pulse at the output port. The delay introduced by the stub depends on l_4 and the phase velocity of the CPW forming the stub. Therefore, the optimal time delay corresponds to half of the incident pulse width. The incident pulse peak must align at the junction with the beginning of the inverse-polarity reflected pulse to create the sharpest transition between the two pulse peaks without loss in peak voltage.

5) Tuning of the Current Source Supply: The current supply ensures that the SRD is forward biased in the absence of the trigger. The trigger introduces a short-time reversed bias, which leads to the diode producing the Gaussian pulse. In [14], a 30-mA current supply is suggested, but no justification is provided. Here, we demonstrate that the current-supply value is critically important for the pulse bandwidth and must be tuned according to the desired specifications. Our prototypes include the R14 resistance (see Fig. 5), which is varied for values between 0 and 21 Ω. This resistance maps into current values from 10 to 200 mA through

$$I_{\text{SOURCE}} = 10\ \mu\text{A} \cdot \frac{\text{R16}}{\text{R14 + R15}} + 10\ \mu\text{A} \tag{1}$$

where R16 = 49.9 kΩ and R15 = 2 Ω. It is found that a minimum resistance of R14 = 8.5 Ω is required to see substantial improvement at higher frequencies with minimal change at lower frequencies. This resistance maps into a 47.5-mA current-source supply. The impact of the respective parameter tuning is illustrated in Section III in terms of the pulse performance metrics defined.

III. PULSE PERFORMANCE METRICS OF THE UWB GENERATOR

A. Definitions of Pulse Metrics

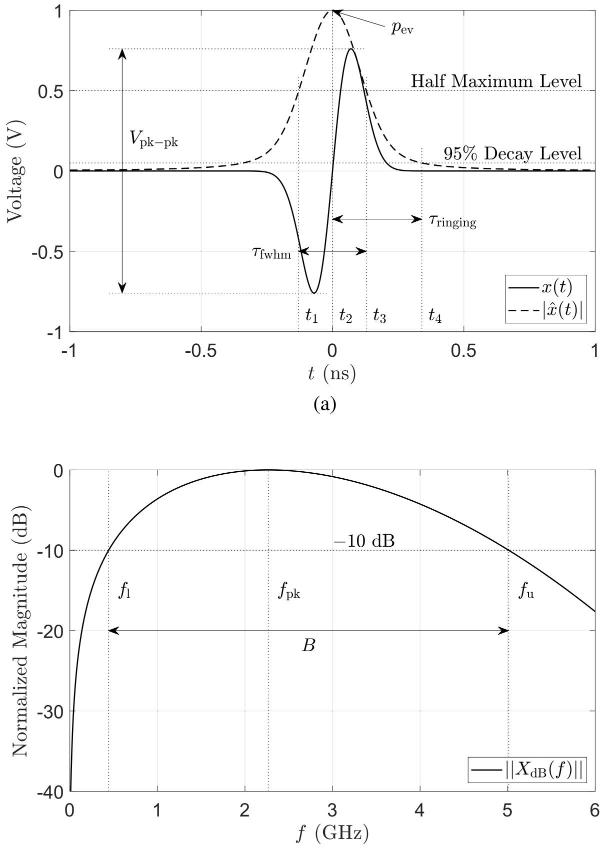

(a)

(b)

Fig. 8. Pulse metrics: (a) temporal domain and (b) spectral domain.

The signal measured by the high-speed sampling oscilloscope [45] in the temporal domain is denoted as $x[n]$. Assuming that $x[n]$ is sufficiently densely sampled to represent the real analog signal, $x(t)$, a complex analytical signal can be approximated through the Hilbert transform[2] [46]. The analytical signal [46]–[48], $\hat{x}(t)$, is defined as

$$\hat{x}(t) = x(t) + j\mathcal{H}\{x(t)\} \tag{2}$$

where the analytical Hilbert envelope

$$|\hat{x}(t)| = \sqrt{x(t)^2 + \mathcal{H}\{x(t)\}^2} \tag{3}$$

estimates accurately the envelope of $x(t)$. Both $x(t)$ and $|\hat{x}(t)|$ are used to evaluate the picosecond pulse generator. Here, the *hilbert* MATLAB function [49] is used.

Fig. 8 illustrates the following pulse metrics.

1) Peak-to-Peak Voltage: The peak-to-peak voltage is a measure of the pulse strength

$$V_{\text{pk-pk}} = |\max\{x(t)\} - \min\{x(t)\}|. \tag{4}$$

2) Full-Width at Half-Maximum: The FWHM is defined by the width at half maximum of the analytical Hilbert envelope $|\hat{x}(t)|$ [48]. It is a measure of the temporal impulse width but also relates to the spectral bandwidth. The peak (or maximum) of the analytical envelope is defined as $p_{\text{ev}} = \max\{|\hat{x}(t)|\}$, whereas the FWHM is

$$\tau_{\text{FWHM}} = t_3\big|_{|\hat{x}(t_3)|=p_{\text{ev}}/2} - t_1\big|_{|\hat{x}(t_1)|=p_{\text{ev}}/2}. \tag{5}$$

---

[2] The Hilbert transform $\mathcal{H}\{\cdot\}$ of a time-domain signal $x(t)$ is $\mathcal{H}\{x(t)\} = x(t) * 1/\pi t$, where $*$ is convolution, whereas, in the Fourier domain, $\mathcal{H}\{X(f)\} = -j\text{sgn}(f)X(f)$, where $\text{sgn}(f)$ is the signum function [47].

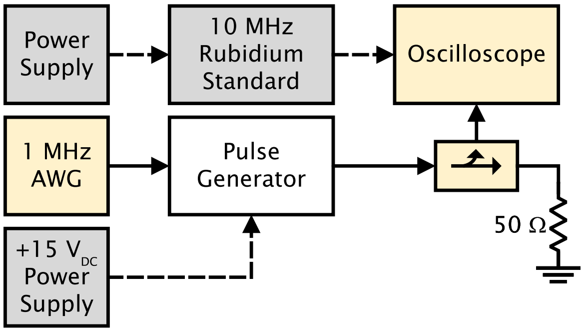

Fig. 9. General measurement test setup for pulse metric evaluation.

3) Late-Time Ringing: Ringing within a pulse waveform is undesirable. It is a result of component resonances and multiple reflections in interconnects [48]. The duration of the ringing, τ_{ringing}, is defined as the time required for the Hilbert envelope peak to decay below a given level α

$$\tau_{\text{ringing}} = t_4\big|_{|\hat{x}(t_4)|=\alpha p_{\text{ev}}} - t_2\big|_{|\hat{x}(t_2)|=p_{\text{ev}}} \tag{6}$$

where $0 \leq \alpha \leq 1$. We use $\alpha = 0.05$ corresponding to a 95% decay level. It is desirable to shorten the ringing time to ensure that most of the energy is contained within the main pulse.

4) 10-dB Bandwidth: The 10-dB bandwidth, B, is defined through the spectral magnitude $|X(f)|$, where $X(f)$ is the fast Fourier transform (FFT) of the measured signal $x(t)$. Note that $x(t)$ is passed through a Hamming window prior to the FFT. The normalized spectral magnitude in the logarithmic scale is

$$\|X_{\text{dB}}(f)\| = 20\log_{10}(|X(f)|) - \max\left\{20\log_{10}(|X(f)|)\right\}. \tag{7}$$

The 10-dB bandwidth is then defined as

$$B = f_{\text{u}} - f_{\text{l}} \text{ s.t. } ||X_{\text{dB}}\left(f|_{f_{\text{l}}\leq f \leq f_{\text{u}}}\right)|| \geq -10 \text{ dB} \tag{8}$$

where f_{l} and f_{u} define the lower and upper frequency bounds.

The bandwidth computed with (8) is also confirmed using the power spectrum density (PSD) estimation based on *Welch's* method [50]. The *pwelch* MATLAB function [51] is used to return the PSD estimate of $x(t)$. The function divides $x(t)$ into the longest possible segments to obtain eight segments with 50% overlap. A Hamming window is also applied to each segment.

5) Fractional Bandwidth: The FBW, b_{f}, is a common figure of merit for UWB devices defined as the ratio of the absolute bandwidth B and the center frequency f_{c}

$$b_{\text{f}} = \frac{B}{f_{\text{c}}} = 2\left(\frac{f_{\text{u}} - f_{\text{l}}}{f_{\text{u}} + f_{\text{l}}}\right) = 2\left(\frac{b_{\text{fr}} - 1}{b_{\text{fr}} + 1}\right) \tag{9}$$

where $b_{\text{fr}} = f_{\text{u}}/f_{\text{l}}$ is the FBW ratio.

B. Measurement Procedures

The measurement setup used for the generator evaluation is shown in Fig. 9. A 10-MHz rubidium standard [52] is used as a frequency standard for the 50 giga-samples per second (GSPS) real-time sampling oscilloscope [45], which has a 50-Ω input and a built-in analog front-end filter with 16-GHz bandwidth. The rubidium standard is an accurate frequency reference for the oscilloscope's internal sampling logic. A 10-dB direction coupler [53] is used to measure the picosecond pulse while protecting the measurement instrument's front end. The coupler's through port is loaded with a 50-Ω load, while the coupled port is connected to the oscilloscope. A 1-MHz square-wave trigger is generated from the arbitrary waveform generator (AWG) built in the oscilloscope [54]. The pulse metrics (see Section III-C) are extracted from a waveform, which is the average of 1024 pulses.

C. Evaluation of the UWB Generator Pulse Metrics

As discussed in Section II, the critical factors impacting the generator's performance are the current supplied by the current source and the stub length l_4. The current-source resistance (R14) regulates the supplied current. Thus, the generator's output has been evaluated for R14 values between 0 and 21 Ω along with two stub lengths, $l_4 = 10.45$, 11.95 mm.

Fig. 10 shows the peak-to-peak voltage *versus* the R14 values for the two stub lengths. The circle points indicate the measurement samples. It is observed that the longer stub length results in a marginal increase in the peak-to-peak voltage. However, the current-source resistance has a marked impact. The R14 values between 2 and 14 Ω provide the largest peak-to-peak voltage (exceeding 10 V).

Fig. 11 reports the FWHM pulsewidth dependence on the R14 value and the stub length. The strong impact of the current supply is again observed. A larger R14 setting (smaller supply current, I_{SOURCE}) decreases the FWHM from 340 to 260 ps. Since a narrow pulse width leads to the UWB performance, an R14 setting of 10 Ω or larger is desirable. Also, it is evident that the stub length plays little to no role in the FWHM pulse width. This is expected since the difference in the two stub lengths leads to reflection delays, which are well below the oscilloscope's 20-ps real-time sampling step.

The late-time ringing dependence on R14 and the stub length is shown in Fig. 12. At low current-source resistance settings, the stub length does not play a vital role in reducing the late-time ringing. However, at higher resistance settings, the longer stub length reduces the ringing by almost 100 ps. Also, at an R14 setting of 14 Ω, a substantial improvement in the late-time ringing for a 10.45-mm stub length seems to occur. However, this is an outlier due to the choice of α in (6) where the Hilbert envelope quickly dips below that threshold for a single sample and quickly returns above it. By varying the decay level (α), it was seen that the current-source resistance and stub length only marginally improve the late-time ringing.

Figs. 13 and 14 show the results of the 10-dB bandwidth and FBW analysis. These figures are divided into two subfigures, (a) and (b), which show the metrics for the 10.45- and 11.95-mm stub lengths, respectively. Fig. 13 shows the upper and lower frequency bounds resulting from the FFT method in black-solid lines, with the 10-dB bandwidth shaded in light green. The PSD method is also plotted for reference using the blue dashed-dotted lines. These metrics were plotted against various current-source resistance values similar to the temporal metrics. The vertical black dashed lines show the occupied

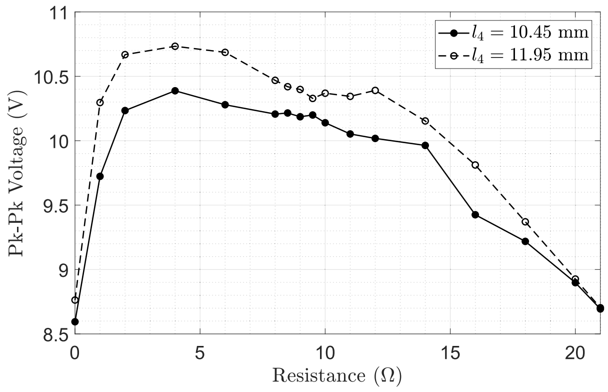

Fig. 10. Peak-to-peak voltage *versus* current-source resistance (R14) and two stub lengths.

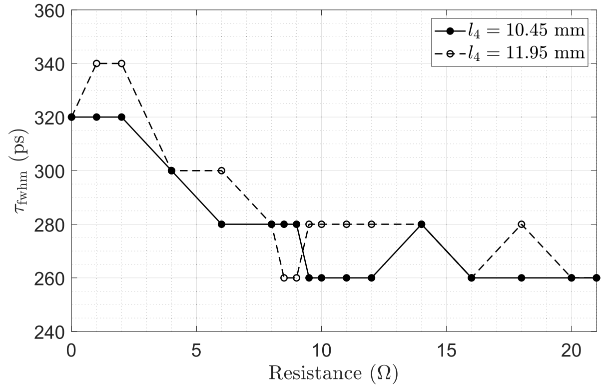

Fig. 11. FWHM *versus* current-source resistance (R14) and two stub lengths.

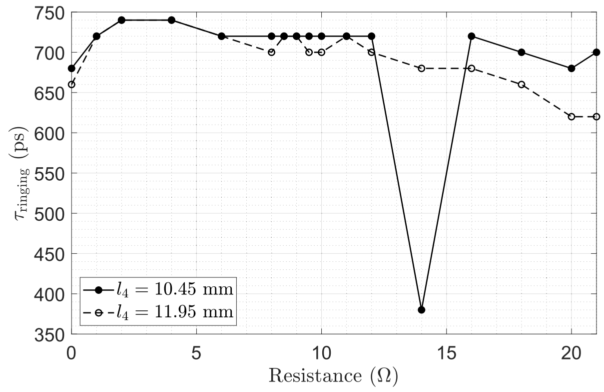

Fig. 12. Ringing *versus* current-source resistance (R14) and the stub lengths ($\alpha = 0.05$).

bandwidth per resistance setting. The horizontal red dotted lines show our desired lower and upper frequency limits of 500 MHz and 5 GHz. We observe an increase in the 10-dB bandwidth for a current-source resistance setting above 8.5 Ω (at least 47.5-mA current supply). A larger resistance setting results in a broader 10-dB bandwidth, which aligns with Fig. 11, showing that the pulse width decreases. It can be seen that, by varying the stub length, only the upper frequency limits are changed. In our case, a shorter stub length is preferred as it easily covers the desired bandwidth for various current-source settings.

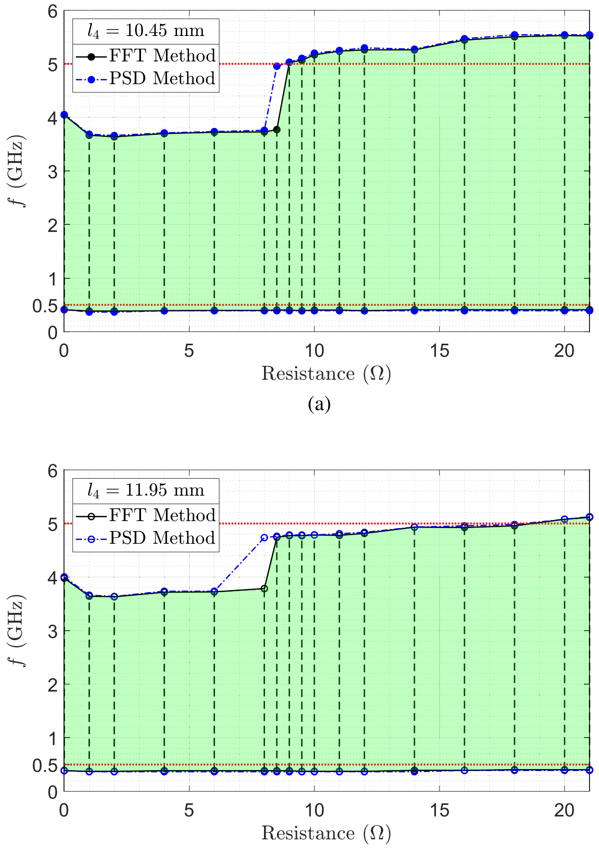

(a)

(b)

Fig. 13. 10-dB bandwidth *versus* current source resistance (R14) settings for two stub lengths: (a) 10.45 and (b) 11.95 mm.

Fig. 14 shows an alternative way of visualizing the picosecond pulse generator's bandwidth through the FBW ratio. Again, the FFT results are shown as the black solid line, while the blue dashed-dotted line shows the PSD method results. The red dotted line shows the desired 1:10 FBW ratio. These subfigures show that the design easily achieves a 1:9 FBW for any current-source setting at both stub lengths. However, if a 1:10 FBW is desirable, a minimum current-source resistance value of 8.5 **Ω** is required no matter the stub length. It is important to note that, with proper tuning, it is possible to achieve FBW ratio as high as 1:13.

IV. JITTER AND NOISE PERFORMANCE METRICS OF THE UWB GENERATOR

A. Definitions of Jitter Metrics

Jitter metrics characterize a signal's timing variation for a set of edges from their ideal location, i.e., they measure the signal's phase stability. Here, we introduce the analysis of a pulse jitter at the generator's output using the known input trigger jitter, as shown in Fig. 15. Both absolute and relative jitter [25]–[27] are evaluated with the available input and are then used in the pulse jitter metric.

1) Absolute Trigger Jitter: The absolute jitter of the generator's input (trigger jitter) is evaluated using standard definitions [25]–[27]. The trigger input is a periodic clock signal

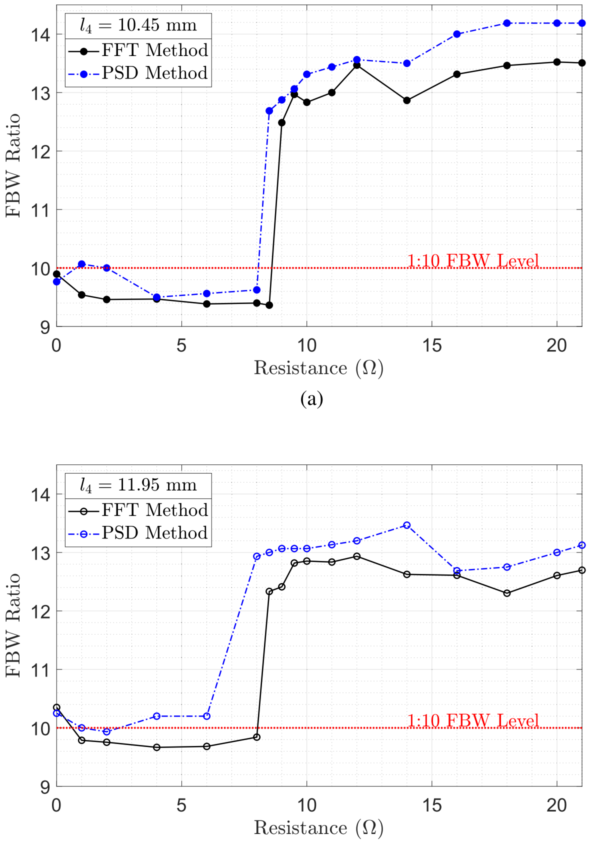

(a)

(b)

Fig. 14. FBW *versus* current source resistance (R14) settings for two stub lengths: (a) 10.45 and (b) 11.95 mm.

with an ideal period of T. The absolute jitter is defined as a discrete-time random sequence, $\mathbf{a}$, where the kth element is denoted as a_k. The trigger jitter is the time displacement between the kth edges of the real clock with respect to the corresponding edge of the ideal clock [25]. The kth edge of the ideal clock can be determined, assuming that the edges do not change with time and are spaced by exactly T. Therefore, the absolute jitter at the kth sample, a_k, is defined as

$$a_k = t_k - kT. \tag{10}$$

Here, t_k denotes the time instance where the real clock edge reaches half of its full amplitude. The trigger jitter is used as our reference and is denoted as $\mathbf{a}_{\mathrm{REF}}$ hereafter.

A probability density function (PDF) histogram for the rising edge of the trigger input is constructed from 10 000 waveforms to produce a statistical model over multiple clock periods. This histogram, which describes the absolute trigger jitter, provides three possible jitter metrics. The first metric is the standard deviation jitter (also known as rms jitter), which is the standard deviation σ of the histogram. The second metric is the peak-to-peak jitter, which is the maximum timing error defined by the minimum and maximum values on the abscissa of the histogram. However, since jitter noise is theoretically an unbounded Gaussian PDF, the length of the taken measurements drives the result. Due to this unbounded nature, it is better to bound the histogram by 6σ, representing 99.6% of the statistical distribution. Therefore, the third and final metric is the six-sigma (6σ) jitter, which is the $\pm 3\sigma$ standard deviation.

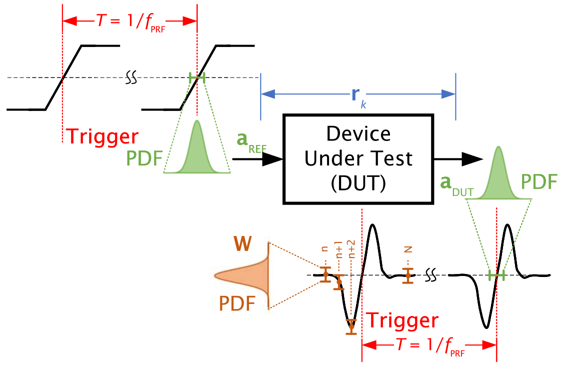

Fig. 15. Jitter (green for $\mathbf{a}$ and blue for $\mathbf{r}$) and noise (orange for $\mathbf{w}$) metrics used for evaluation.

2) Absolute Pulse Jitter: Although the output of the picosecond pulse generator does not contain clock-like rising and falling edges, it does produce a periodic waveform, which allows for phase-stability evaluation. Here, we propose to use the temporal point where the pulse voltage crosses the 0-V reading while swinging between minimum-to-maximum peaks. The ideal pulse period is determined by the period, T, of the input trigger. Thus, we can use (10) to define the pulse jitter as $\mathbf{a}_{\mathrm{DUT}}$, where t_k is the kth pulse zero-crossing point.

3) Relative Jitter: In contrast to absolute jitter, which compares a real clock to an ideal one, the relative-jitter metric compares two real clocks with the same average period T. One of these real clocks serves as a reference. Similar to absolute jitter, the relative jitter is viewed as a discrete-time random process $\mathbf{r}$, where the element r_k is the time displacement of the kth edge of the device under test (DUT) with respect to that of the reference clock [25]. The relative jitter can be expressed in terms of the two signals' absolute jitter

$$\mathbf{r} = \mathbf{a}_{\mathrm{DUT}} - \mathbf{a}_{\mathrm{REF}}. \tag{11}$$

Here, the same σ, 6σ, and peak-to-peak jitter metrics apply. Note that a negative relative jitter result means that the DUT decreases the output jitter compared to the reference.

4) Jitter Measurements: Fig. 16 depicts the jitter measurement setup for each section of the picosecond pulse generator. During development, the generator has been broken down into separate hardware modules: the jitter cleaner, the trigger amplifier, and the driver along with the pulse generator circuit. The modules are accessed through SMA connectors. Note that these modules are amalgamated into a single PCB prototype, which has been presented in Section II.

As indicated in Fig. 16, the absolute jitter values are denoted as $\mathbf{a}_{\mathrm{DUT}}$, where DUT designates the measured module. The blue dashed, green dotted, and red dashed-dotted arrows indicate the output signals fed to the oscilloscope port. The blue arrows are associated with $\mathbf{a}_{\mathrm{TRIG}}$, $\mathbf{a}_{\mathrm{JC}}$, and $\mathbf{a}_{\mathrm{UWB5}}$, i.e., the absolute jitter at the outputs of the input trigger, the jitter cleaner, and the whole generator (as shown in Fig. 6). The green arrow is associated with the total absolute jitter

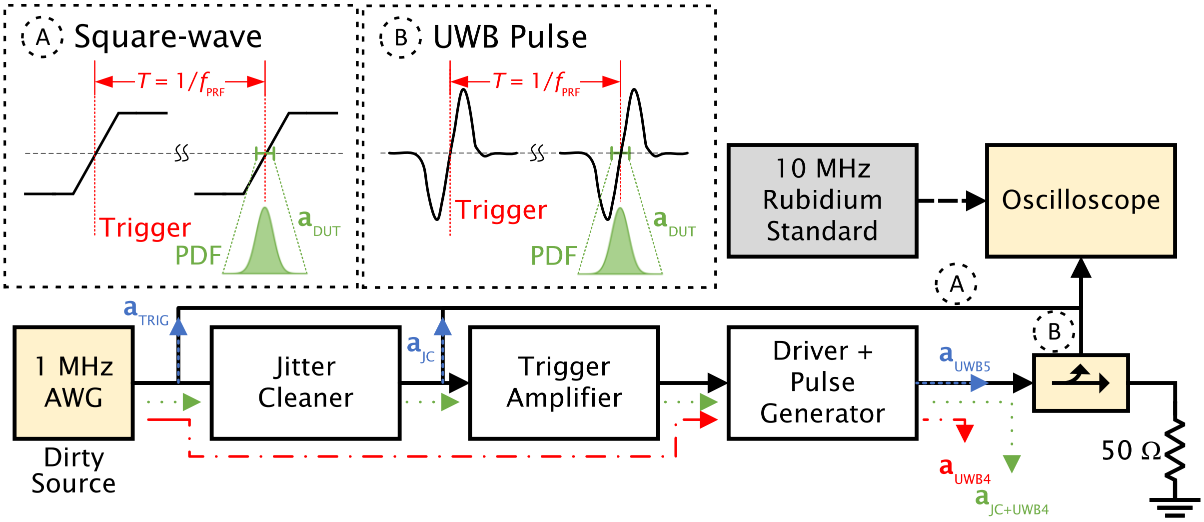

Fig. 16. Measurement setup used for the jitter metric evaluation.

$\mathbf{a}_{\text{JC+UWB4}}$ of the cascaded prototype. The $\mathbf{a}_{\text{JC+UWB4}}$ measurement, compared to $\mathbf{a}_{\text{UWB5}}$, is a verification that the integrated, and the cascaded prototypes are comparable. The red arrow corresponds to the absolute jitter $\mathbf{a}_{\text{UWB4}}$ of the driver and pulse generator circuit, which bypasses the jitter cleaner and the trigger amplifier. Note that the oscilloscope is directly connected to the outputs of the AWG trigger and the jitter cleaner, whereas, in the measurements of the generated pulse, it requires the directional coupler for protection. The AWG is used to generate the input trigger and is considered a dirty (not stable) source for this work since its jitter is significant enough to be measured.

The insets A and B in Fig. 16 illustrate the type of waveform measured by the oscilloscope at the outputs of the AWG trigger and the jitter cleaner (A) and the UWB pulse generator (B). The oscilloscope is configured to trigger on the positive slope (first edge). We then delay the signal on the oscilloscope view to capture the next edge following the trigger edge. 10 000 waveforms are obtained and saved for processing offline. A temporal histogram is created from the 10 000 waveforms by finding the closest discrete-time sample to a threshold crossing using a sinc ($\sin(t)/t$) interpolation. The threshold is half the waveforms amplitude for the square-wave trigger signals, whereas, for the UWB pulse, the threshold is 0-V. The σ, 6σ, and peak-to-peak absolute jitter are obtained from the histogram.

B. Jitter Evaluation of the UWB Generator

Tables III and IV show the absolute and relative jitter results for the prototype with R14 = 14 Ω and l_4 = 10.45 mm. Each table contains the standard deviation (σ), 6σ, and pk-pk jitter results. Referring back to Fig. 16, the relationship between the circuits and measurement location of Table III can be understood. The absolute jitter of the trigger source ($\mathbf{a}_{\text{TRIG,3.3 V}}$ or $\mathbf{a}_{\text{TRIG,5.0 V}}$) has a standard deviation on the orders of 150 ps. When this trigger is applied to the proposed generator without the jitter cleaners, we see a relative (REF = $\mathbf{a}_{\text{TRIG,5.0 V}}$ and DUT = $\mathbf{a}_{\text{UWB4}}$) jitter decrease in the standard deviation by 95.17 ps. The resulting standard deviation of the output jitter for the driver and pulse generator circuit is 52.83 ps ($\mathbf{a}_{\text{UWB4}}$). This means that the pulse jitter standard deviation is on the order of 10 GSPS (or 10 GHz), which is the Nyquist sampling rate required to reconstruct the 5-GHz frequency components. In this case, the total arrival time uncertainty of the pulse can vary as much as the 6σ or pk-pk jitter, which is on the order of 300–400 ps. This is six to eight times the Nyquist sampling rate and is not desirable.

The introduction of the jitter cleaner provides a substantial improvement on the pulse jitter of the picosecond pulse generator. In measurements of generators that contain a jitter cleaner ($\mathbf{a}_{\text{JC+UWB4}}$ and $\mathbf{a}_{\text{UWB5}}$), either as an evaluation board or embedded on the PCB, we see a standard deviation of approximately 1.6 ps and 6σ or pk-pk jitter on the orders of 10 ps. Therefore, there is 50 times reduction due to the jitter cleaner ($\mathbf{a}_{\text{TRIG,3.3 V}}$ *versus* $\mathbf{a}_{\text{JC}}$) and two times reduction due to the generator circuit design ($\mathbf{a}_{\text{JC}}$ *versus* $\mathbf{a}_{\text{JC+UWB4}}$, $\mathbf{a}_{\text{UWB5}}$). It should be mentioned that these results include the oscilloscope's typical rms (standard deviation) trigger jitter of 1 ps [45]. The inclusion of the jitter cleaner enables the generator to maintain stability within the Nyquist sampling rate necessary for reconstruction.

C. Definitions of Noise Metrics

We propose a method to evaluate the generator's voltage noise so that it excludes a noise contribution from the measurement setup. Here, we are primarily concerned with voltage amplitude uncertainty due to internal noise produced within the generator. This noise is usually measured through the rms (one σ) of the PDF since it is considered random and modeled by a Gaussian distribution [55].

In order to evaluate the generator's performance, it is crucial to deembed the noise produced by the measurement setup. This is indeed possible assuming that: 1) the measurement setup for the DUT and that for the inherent setup noise are the same and 2) the DUT noise is greater than that in the measurement reference. It is also necessary to assume that

TABLE III
RESULTS OF THE ABSOLUTE JITTER ANALYSIS

Measurement	Std. Dev. (σ), (ps)	6-Sigma (6σ), (ps)	Pk-Pk (ps)
$\mathbf{a}_{\text{TRIG,3.3V}}$ [$\mathbf{a}_{\text{TRIG,5.0V}}$]	154.2 [148.0]	925.2 [888.0]	1240.0 [1200.0]
$\mathbf{a}_{\text{JC}}$	3.07	18.42	23.75
$\mathbf{a}_{\text{UWB4}}$	52.83	317.0	388.0
$\mathbf{a}_{\text{JC+UWB4}}$	1.658	9.948	12.5
$\mathbf{a}_{\text{UWB5}}$	1.653	9.918	11.25

TABLE IV
RESULTS OF THE RELATIVE JITTER ANALYSIS

Measurement				
REF	DUT	Std. Dev. (σ), (ps)	6-Sigma (6σ), (ps)	Pk-Pk (ps)
$\mathbf{a}_{\text{TRIG,3.3V}}$	$\mathbf{a}_{\text{JC}}$	-151.13	-906.78	-1216.25
$\mathbf{a}_{\text{TRIG,5.0V}}$	$\mathbf{a}_{\text{UWB4}}$	-95.17	-571.02	-812.0
$\mathbf{a}_{\text{JC}}$	$\mathbf{a}_{\text{JC+UWB4}}$	-1.412	-8.472	-11.25
$\mathbf{a}_{\text{JC}}$	$\mathbf{a}_{\text{UWB5}}$	-1.417	-8.502	-12.5
$\mathbf{a}_{\text{TRIG,3.3V}}$	$\mathbf{a}_{\text{JC+UWB4}}$	-152.542	-915.252	-1227.5
$\mathbf{a}_{\text{TRIG,3.3V}}$	$\mathbf{a}_{\text{UWB5}}$	-152.547	-915.282	-1228.75

the noise sources of the setup and the DUT are uncorrelated, and their statistical models are available. Therefore, two noise models are developed and used for this analysis: 1) for the measurement setup (system noise) and 2) for the DUT (pulse generator noise). As explained next, these models are based on histograms of the PDF generated at each temporal sample for $M = 10\,000$ pulse waveforms.

Here, we propose to define noise as a function of the temporal sample n since the noise is expected to increase within the pulse duration. Thus, the *voltage noise* is quantified by the discrete-time random process, $\mathbf{w}$, where the element w_n is the variance σ_n^2 of the set of M pulse waveforms at the nth time sample. In all results presented hereafter, the waveforms contain $N = 200$ samples, i.e., $n = [1, \ldots, 200]$.

1) System Noise Measurement: A directional coupler [53] is required to protect the input of the oscilloscope while measuring the pulse generator (the DUT). Therefore, to evaluate the system noise, the oscilloscope is connected directly to the coupled port, which incurs a 10-dB loss. Two 50-Ω loads terminate the input and through ports. The voltage deviation is set to 400 mV/div. Note that the voltage-deviation setting affects the oscilloscope voltage resolution. Also, the 10-dB external attenuation due to the direction coupler affects the noise measurements. We assume that this attenuation affects the noise similarly in the system and the DUT measurements. This measurement provides the system noise $(\sigma_n^2)_{\text{SYS}}$.

2) Pulse Generator (DUT) Noise Measurement: This time, the generator's output is connected to the directional coupler's input port, while the through port is terminated with a 50-Ω load. The oscilloscope is still connected directly to the coupled port. The voltage deviation of the oscilloscope remains the same as in the system-noise measurement setup. A time window is captured before and after the pulse to characterize the change in the noise metrics between pulse and no-pulse periods. This measurement provides the noise $(\sigma_n^2)_{\text{M}}$, which includes the system noise $(\sigma_n^2)_{\text{SYS}}$ and the noise due to the DUT $(\sigma_n^2)_{\text{DUT}}$, which is to be extracted.

3) System Noise Deembedding Process: The noise of the pulse generator is defined by $(\sigma_n^2)_{\text{DUT}}$, whereas the system measurement noise is $(\sigma_n^2)_{\text{SYS}}$. The total measured noise $(\sigma_n^2)_{\text{M}}$ includes both, which is modeled as

$$\left(\sigma_n^2\right)_{\text{M}} = \left(\sigma_n^2\right)_{\text{DUT}} + \left(\sigma_n^2\right)_{\text{SYS}} + \Sigma_{\text{DUT,SYS}} \tag{12}$$

where $\Sigma_{\text{DUT,SYS}}$ is the covariance between the two signals. Provided that the noise in the DUT signal that in the SYS signal are uncorrelated, and they are both with zero mean, $\Sigma_{\text{DUT,SYS}} = 0$, and (12) simplifies to

$$\left(\sigma_n^2\right)_{\text{M}} = \left(\sigma_n^2\right)_{\text{DUT}} + \left(\sigma_n^2\right)_{\text{SYS}}. \tag{13}$$

Since the system noise is estimated separately under the same test conditions as the DUT, the DUT variance is obtained as

$$\left(\sigma_n^2\right)_{\text{DUT}} = \left(\sigma_n^2\right)_{\text{M}} - \left(\sigma_n^2\right)_{\text{SYS}} \tag{14}$$

and the standard deviation is

$$(\sigma_n)_{\text{DUT}} = \sqrt{\left(\sigma_n^2\right)_{\text{M}} - \left(\sigma_n^2\right)_{\text{SYS}}}. \tag{15}$$

Note that (15) implies that $(\sigma_n^2)_{\text{M}} \geq (\sigma_n^2)_{\text{SYS}}$. If $(\sigma_n^2)_{\text{M}} < (\sigma_n^2)_{\text{SYS}}$, then the generator does not produce measurable additive noise.

D. Noise Evaluation of the UWB Generator

The results of the voltage noise analysis are presented in Fig. 17. A histogram heatmap generated by the $10\,000$ waveforms is shown in Fig. 17(a). Red and blue indicate high and low probabilities of the waveform values, respectively. Note

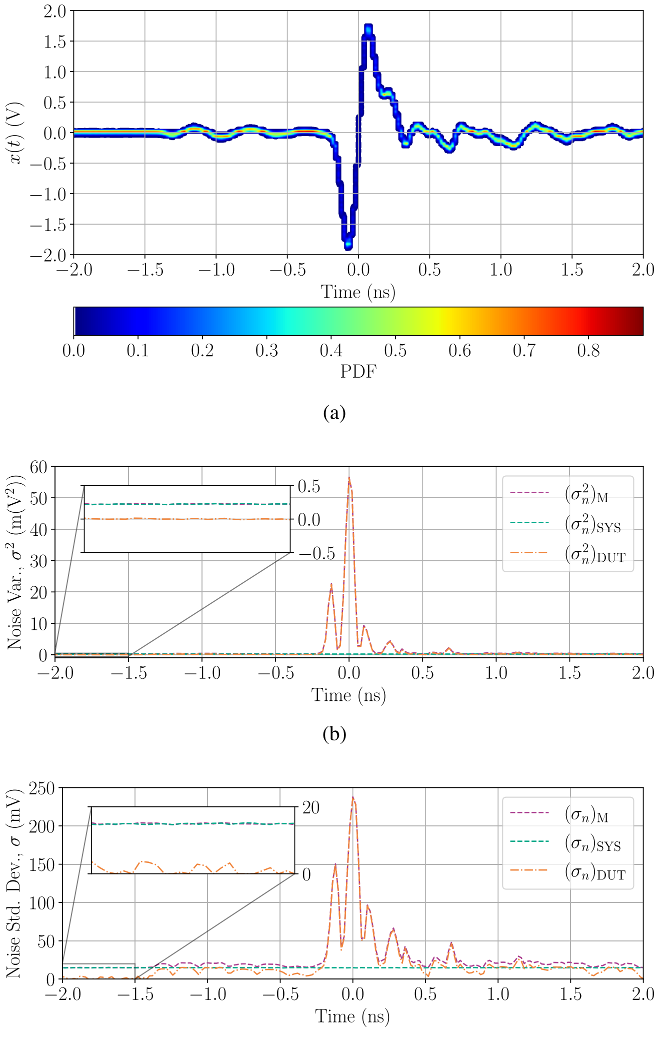

(a)

(b)

(c)

Fig. 17. Noise analysis with 10-dB external attenuation and an oscilloscope voltage division of 400 mV/div. (a) Picosecond pulse generator waveform histogram heatmap of 10 000 waveforms overlaid. (b) Noise variance of the histogram of the measured signal [$(\sigma_n^2)_\mathrm{M}$], system noise measurement [$(\sigma_n^2)_\mathrm{SYS}$], and DUT [$(\sigma_n^2)_\mathrm{SYS}$]. (c) Noise standard deviation of the histogram for the same respective measurements.

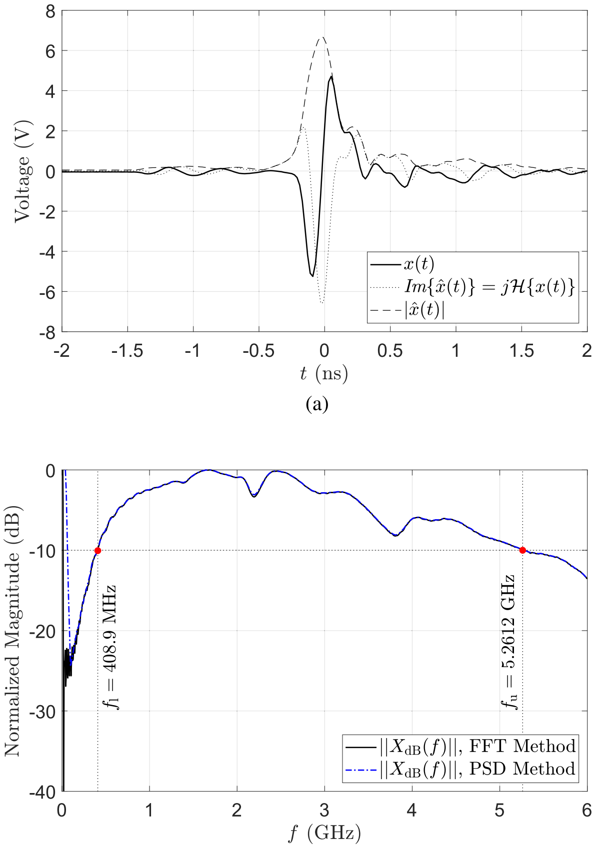

(a)

(b)

Fig. 18. Sample of a pulse generated by the picosecond pulse generator (R14 = 14 Ω and $l_4 = 10.45$ mm). (a) Time-domain plot of the measured pulse ($x(t)$), the imaginary part of the analytical waveform obtained with the Hilbert transform, and the Hilbert envelope. (b) Frequency-domain plot of the measured pulse calculated using the FFT and PSD methods. The −10-dB lower and upper frequency bounds are shown by the red dots.

that these waveforms are obtained with the 10-dB directional coupler, and the 10-dB voltage decrease has not been compensated in the plot. Fig. 17(b) and (c) shows the variance and standard deviation describing the total measured noise, the system noise, and the deembedded DUT noise *versus* time. As expected, within the pulse duration, additive Gaussian noise is present. The mean of the reference noise variance is 0.22 m(V^2), whereas its standard deviation is 14.93 mV. We observe that, during the main pulse transition, the DUT noise increases, e.g., its standard deviation becomes about 16 times greater than the mean of the system-noise standard deviation. Their largest values are seen at the time of the largest voltage swings. However, at the pulse minima and maxima, the voltage is stable to within a standard deviation of 55 mV.

In the timeframe from −2.0 to −1.5 ns, the generator does not produce additive noise, resulting in the presence of system noise only. There are instances within this timeframe, where $(\sigma_n^2)_\mathrm{M} < (\sigma_n^2)_\mathrm{SYS}$, and (15) produces a small imaginary number [$(\sigma_n^2)_\mathrm{DUT}$ not exceeding -0.016 m(V^2)]. In such instances, we enforce a hard zero floor. An intuitive explanation is that, while the transmitter is in an OFF-state or a standby state, its additive noise is not measurable with this setup. Mathematically, the negative DUT noise variance values can be explained through the existence of nonzero positive covariance $\Sigma_\mathrm{DUT,SYS}$ in (12), resulting in corrected forms of (14) and (15)

$$\left(\sigma_n^2\right)_\mathrm{DUT} = \left(\sigma_n^2\right)_\mathrm{M} - \left(\sigma_n^2\right)_\mathrm{SYS} - \Sigma_\mathrm{DUT,SYS} \tag{16}$$

$$(\sigma_n)_\mathrm{DUT} = \sqrt{\left(\sigma_n^2\right)_\mathrm{M} - \left(\sigma_n^2\right)_\mathrm{SYS} - \Sigma_\mathrm{DUT,SYS}}. \tag{17}$$

This covariance term, however, cannot be obtained as it is inherent to the measurement setup.

V. DISCUSSION

It is evident that the proposed generator design has to strike a balance between the maximum peak-to-peak voltage and the maximum spectral bandwidth. The choices of the current-source supply current and the stub length are crucial. A smaller current supply (larger R14 resistance) results in a

TABLE V

COMPARISON WITH PRIOR LITERATURE

Metric	This work	[13]	[14]	[22]	[17]	[23]	[16]	[18]	[19]	[20]	[6]	[21]
Pulse Type	MC	MC	G/MC	G$^{\mathrm{n}}$	G/MC	G$^{\mathrm{n}}$	G	G	G	G	MC	G/MC
Technology	SRD	SRD	SRD	CMOS	SRD	CMOS	SRD	SRD	SRD	SRD	SRD	SRD
PRF (MHz)	1	1	3.125 kHz – 20	10 – 50	10 – 100	33	NA	10	10	0.1	1000	10
$V_{\text{pk-pk}}$ (V)	9.9633	9.477	27 / 25	0.425	6.8 / 4.6, 1.2 / 0.7	2.12	3.95, 4.1, 3.9, 3.92	1.67 / 0.83	1.586	6.4	0.3	1.3 / 1.6
p_{ev} (V)	6.677	NA	NA	NA	NA	NA	NA	NA	NA	NA	NA	NA
τ_{FWHM} (ps)	280	NA	180†/ 500‡	600‡	220, 60†	500‡	34, 24, 24, 34†	214, 153†	286†	620†	330 – 380	300 – 1000‡
τ_{ringing} (ps)	380	NA	NA	NA	NA	NA	NA	NA	NA	NA	NA	NA
f_l (GHz)	0.4089	0.4395	NA	3.8	0.5 / 1	3.6¶	NA	NA	NA	NA	2.5, 2¶	NA
f_u (GHz)	5.2612	3.5889	NA	8.8	3 / 13	11.1¶	NA	NA	NA	NA	11, 10.6¶	NA
f_c (GHz)	2.8351	3.8087	NA	6.3¶	1.75 / 7¶	7.35¶	NA	NA	NA	NA	6.75, 6.3¶	NA
B (GHz)	4.8523	3.1494	NA	5	2.5 / 12¶	7.5	NA	NA	NA	NA	8.5, 8.6¶	NA
b_{f}	1.712	0.8269¶	NA	0.7937¶	1.429 / 1.714¶	1.020¶	NA	NA	NA	NA	1.259, 1.365¶	NA
b_{fr}	12.8657	8.166¶	NA	2.316¶	6 / 13¶	3.083¶	NA	NA	NA	NA	4.4, 5.3¶	NA
$\mathbf{a}_k$ (ps)	1.653	1.32‖	NA	NA	NA	NA	NA	NA	NA	NA	NA	NA
$(\sigma_n^2)_{\text{DUT}}$ (m(V)^2)	46.42	NA	NA	NA	NA	NA	NA	NA	NA	NA	NA	NA
$(\sigma_n)_{\text{DUT}}$ (mV)	215.45	324.0‖	NA	NA	NA	NA	NA	NA	NA	NA	NA	NA

† Gaussian pulse FWHM value reported. ‡ Full pulse width value reported, calculation criterion unknown.
¶ Estimated based on reported figures but not explicitly stated in cited text. ‖ Different calculation criterion was used.
NA stands for Not Available.

shorter pulse containing higher frequency components. On the other hand, a larger current supply (smaller R14 resistance) is required to produce a larger peak-to-peak voltage. Similarly, a longer stub length (l_4) produces a larger peak-to-peak voltage, whereas a shorter length results in higher frequency components. Based on these observations, a picosecond pulse generator has been tuned to meet our design criteria of a 1:10 FBW ranging from 500 MHz to 5 GHz with a 10-V peak-to-peak voltage.

Fig. 18 presents the output pulse of the tuned prototype, where the current-source resistance (R14) is 14 Ω and the stub length (l_4) is 10.45 mm. Fig. 18(a) shows the picosecond pulse in the time domain with a black solid line. The imaginary part (see (2)) is also plotted along with the resulting Hilbert envelope. Fig. 18(b) shows the normalized FFT and PSD pulse spectra along with the −10-dB bandwidth limits.

All performance metrics, as defined and proposed in this work, are presented in the first column of Table V. The tuned generator has a band extending from 408.9 MHz to 5.2612 GHz with FBW (b_{f}) of 1.7 and FBW ratio (b_{fr}) of 1:12.9. At the same time, it achieves a 10-V peak-to-peak voltage.

The inclusion of the jitter cleaner dramatically reduces the generator's jitter to only a few picoseconds. With an output absolute jitter standard deviation of 1.6 ps, the design shows a 100× improvement compared to the input trigger. The voltage noise of the generator is consistent, while a pulse is being generated. When the generator is in an OFF-state or a standby state, before and after a pulse generation, the internal circuitry generates no additive noise. At the minima and maxima of the pulse, the waveform is consistent within a standard deviation of 55 mV, thus ensuring reproducible peak-to-peak voltage and peak power. Overall, the proposed generator circuit has been shown to produce a stable, jitter-free monocycle pulse.

Table V compares the proposed design with similar designs reported in the literature. The pulse types are designated as Gaussian (G), Monocycle (MC), and high-order Gaussian derivatives (G$^{\mathrm{n}}$). The "/" in the table helps separate metrics when multiple pulse types are reported, whereas "," indicates multiple results per pulse type. "NA" indicates that the metric has not been reported.

Table V illustrates the superior performance of the proposed generator. It also shows the lack of complete performance evaluation in previous work, especially in terms of jitter and voltage noise. This is due to the lack of an agreed-upon set of metrics in the UWB community. The metrics proposed here aim to fill this gap. The pulse stability (jitter and noise) has never been reported in prior publications, yet these are crucial metrics of a generator's performance. It is our hope that the complete set of metrics proposed here will lead to an all-inclusive figure of merit (FOM), which could be used in the future to compare the various pulse-generator designs.

VI. CONCLUSION

An SRD-based picosecond pulse generator is designed to generate a stable differentiated Gaussian waveform with 1:10 FBW ratio, bandwidth from 500 MHz to beyond 5 GHz at the −10-dB level, and 10-V peak-to-peak voltage. The tuning strategies are discussed, which lead to a significant improvement in pulse bandwidth without loss of peak-to-peak voltage compared to the designs reported in the literature. It is found that the critical factors impacting the pulse metrics are the amount of current supplied to the pulse generating circuit by the dc current source and the length of the stub responsible for the pulse differentiation. A complete set of metrics is defined for the performance analysis of the UWB pulse generator with the introduction of new metrics for jitter and noise analysis. It is determined that the major contribution to the generator's jitter is due to the input trigger source. The inclusion of a jitter cleaner is shown to result in a dramatic improvement in pulse stability.

REFERENCES

[1] *First Report and Order, Revision of Part 15 of Commission's Rule Regarding UWB Transmission System FCC 02–48*, Federal Commun. Commission (FCC), Washington, DC, USA, Apr. 2002.

[2] *Devices Using Ultra-Wideband (UWB) Technology*, Ind. Canada, Spectr. Manage. Telecommun., Ottawa, ON, Canada, Apr. 2009.

[3] *ECC Decision (06)04: The Harmonised Conditions for Devices Using Ultra-Wideband (UWB) Technology in the Bands Below 10.6 GHz*, Electron. Commun. Committee (ECC), Eur. Conf. Postal Telecommun. Admin. (CEPT), Copenhagen, Denmark, Mar. 2006.

[4] J. S. Lee, C. Nguyen, and T. Scullion, "A novel, compact, low-cost, impulse ground-penetrating radar for nondestructive evaluation of pavements," *IEEE Trans. Instrum. Meas.*, vol. 53, no. 6, pp. 1502–1509, Dec. 2004.

[5] F. Rodriguez-Morales *et al.*, "An improved UWB microwave radar for very long-range measurements of snow cover," *IEEE Trans. Instrum. Meas.*, vol. 69, no. 10, pp. 7761–7772, Oct. 2020.

[6] R. Thai-Singama, F. Du-Burck, and M. Piette, "A low-cost UWB pulse generator for medical imaging, through-wall imaging and surveillance systems," in *Proc. IEEE Asia–Pacific Conf. Appl. Electromagn. (APACE)*, Melaka, Malaysia, Dec. 2012, pp. 45–50.

[7] A. D. Pitcher, J. J. McCombe, E. A. Eveleigh, and N. K. Nikolova, "Compact transmitter for pulsed-radar detection of on-body concealed weapons," in *IEEE MTT-S Int. Microw. Symp. Dig.*, Philadelphia, PA, USA, Jun. 2018, pp. 919–922.

[8] E. A. Eveleigh, "Development of an ultra-wideband (UWB) pulse generator and printed antenna for concealed weapons detection radar," M.A.Sc. Thesis, Dept. Elect. Comput. Eng., McMaster Univ., Hamilton, ON, Canada, Jul. 2020.

[9] N. K. Nikolova, "Microwave biomedical imaging," in *Wiley Encyclopedia of Electrical and Electronics Engineering*. Hoboken, NJ, USA: Wiley, Apr. 2014, pp. 1–22.

[10] E. C. Fear, J. Bourqui, C. Curtis, D. Mew, B. Docktor, and C. Romano, "Microwave breast imaging with a monostatic radar-based system: A study of application to patients," *IEEE Trans. Microw. Theory Techn.*, vol. 61, no. 5, pp. 2119–2128, May 2013.

[11] E. Porter, E. Kirshin, A. Santorelli, M. Coates, and M. Popović, "Time-domain multistatic radar system for microwave breast screening," *IEEE Antennas Wireless Propag. Lett.*, vol. 12, pp. 229–232, 2013.

[12] J. Sachs, *Handbook of Ultra-Wideband Short-Range Sensing*, 1st ed. Weinheim, Germany: Wiley, 2012.

[13] A. D. Pitcher, "Compact low-cost ultra-wideband pulsed-radar system," M.A.Sc. Thesis, Dept. Elect. Comput. Eng., McMaster Univ., Hamilton, ON, Canada, Aug. 2019.

[14] P. Protiva, J. Mrkvica, and J. Macháč, "Universal generator of ultra-wideband pulses," *Radioengineering*, vol. 17, no. 4, pp. 74–78, Dec. 2008.

[15] J. McCombe, "Cognitive microwave radar for the stand-off detection of on-body concealed weapons," Comput. Electromagn. Lab., McMaster Univ., Hamilton, ON, Canada, Tech. Rep., CEM-R-70, Mar. 2015.

[16] M. Rahman and K. Wu, "A nonlinear transmission approach to compressing rise and fall time in picosecond pulse generation," *IEEE Trans. Instrum. Meas.*, vol. 70, pp. 1–13, 2021.

[17] R. Feghhi, D. Oloumi, and K. Rambabu, "Tunable subnanosecond Gaussian pulse radar transmitter: Theory and analysis," *IEEE Trans. Microw. Theory Techn.*, vol. 68, no. 9, pp. 3823–3833, Sep. 2020.

[18] R. Feghhi, D. Oloumi, and K. Rambabu, "Design and development of an inexpensive sub-nanosecond Gaussian pulse transmitter," *IEEE Trans. Microw. Theory Techn.*, vol. 67, no. 9, pp. 3773–3782, Sep. 2019.

[19] D. Oloumi and E. Fear, "A picosecond pulse generator using SRD diodes: Design, analysis, and measurements," in *Proc. USNC-URSI Radio Sci. Meeting*, Boston, MA, USA, Jul. 2018, pp. 159–160.

[20] Y. Ahajjam, O. Aghzout, J. M. Catala-Civera, F. Penaranda-Foix, and A. Driouach, "A compact UWB sub-nanosecond pulse generator for microwave radar sensor with ringing miniaturization," in *Proc. 5th Int. Conf. Multimedia Comput. Syst. (ICMCS)*, Marrakech, Morocco, Sep. 2016, pp. 497–501.

[21] C. Zhang and A. E. Fathy, "Reconfigurable pico-pulse generator for UWB applications," in *IEEE MTT-S Int. Microw. Symp. Dig.*, San Francisco, CA, USA, Jun. 2006, pp. 407–410.

[22] X. An, J. Wagner, and F. Ellinger, "An efficient ultrawideband pulse transmitter with automatic On–Off functionality for primary radar systems," *IEEE Microw. Wireless Compon. Lett.*, vol. 30, no. 4, pp. 449–452, Apr. 2020.

[23] S. Gao and K. Moez, "A 2.12-V V_{pp} 11.67-pJ/pulse fully integrated UWB pulse generator in 65-nm CMOS technology," *IEEE Trans. Circuits Syst. I, Reg. Papers*, vol. 67, no. 3, pp. 1058–1068, Mar. 2020.

[24] E. Kaya and K. Entesari, "A broadband CMOS pulse generator for UWB systems," in *Proc. IEEE Radio Wireless Symp. (RWS)*, San Antonio, TX, USA, Jan. 2020, pp. 9–11.

[25] N. Da Dalt and A. Sheikholeslami, *Understanding Jitter and Phase Noise: A Circuits and Systems Perspective*, 1st ed. Cambridge, U.K.: Cambridge Univ. Press, 2018.

[26] *Definitions and Terminology for Synchronization Networks*, Telecommun. Standardization Sector Int. Telecommun. Union (ITU-T), Geneva, Switzerland, Aug. 1996.

[27] *Jitter Specifications for Timing Signals*, Integr. Device Technol., Inc., San Jose, CA, USA, May 2014.

[28] *Si5317 Pin-Controlled 1–711 MHz Jitter Cleaning Clock*, Datasheet Si5317, Silicon Laboratories Inc., Austin, TX, USA, Apr. 2011.

[29] *Innovative DSPPL and MultiSynth Clock Architecture Enables High-Density 10/40/100G Line Card Designs*, Silicon Laboratories Inc., Austin, TX, USA, 2013.

[30] *Wideband, Current Feedback Operational Amplifier With Disable*, Datasheet SBOS226D, Texas Instrum., Dallas, TX, USA, Jul. 2008.

[31] *SN74LVC1G04 Single Inverter Gate*, Datasheet SCES214AD, Texas Instrum., Dallas, TX, USA, Oct. 2014.

[32] *Surface Mount Bias-Tee TCBT-14R+*, Datasheet TCBT-14R+, Mini-Circuits, Brookyn, NY, USA, Apr. 2018.

[33] *Pulse and Waveform Generation With Step Recovery Diodes*, Hewlett Packard, Palo Alto, CA, USA, 1986.

[34] *3313–3 mm Trimpot Triming Potentiometer*, Datasheet 3313, Bourns, Inc., Riverside, CA, USA, Aug. 2019.

[35] *Low Noise Silicon Bipolar RF Transistor*, Datasheet BFP196W, Infineon Technol., Munich, Germany, Apr. 2014.

[36] *Single Silicon RF Schottky Diode*, Datasheet BAT15-03W, Infineon Technol., Munich, Germany, Jun. 2018.

[37] *Silicon Step Recovery Diode*, Datasheet MMDx & SMMDx Series, MACOM Technol. Solutions Inc., Lowell, MA, USA.

[38] *LT3092: 200 mA 2-Terminal Programmable Current Source*, Datasheet LT0217, Linear Technol., Milpitas, CA, USA, Feb. 2009.

[39] *TPS56220x 4.5-V to 17-V Input, 2-A Synchronous Step-Down Voltage Regulator in 6-Pin SOT-23*, Datasheet SLVSD91B, Texas Instrum., Dallas, TX, USA, Sep. 2020.

[40] *LMZ34002 15-W Negative Output Power Module With 4.5-V to 40-V Input in QFN Package*, Datasheet SNVS989C, Texas Instrum., Dallas, TX, USA, Apr. 2018.

[41] *TPS7A470x 36-V, 1-A, 4-μV_{RMS}, RF LDO Voltage Regulator*, Datasheet SBVS204F, Texas Instrum., Dallas, TX, USA, Sep. 2014.

[42] *TPS7A33 −36-V, 1-A, Ultralow-Noise Negative Voltage Regulator*, Datasheet SBVS169D, Texas Instrum., Dallas, TX, USA, Apr. 2015.

[43] *INA233 High-Side or Low-Side Measurement, Bidirectional Current and Power Monitoring With i^2c-, SMBus-, and PMBus-Compatible Interface*, Datasheet SBOS790, Texas Instrum., Dallas, TX, USA, Apr. 2017.

[44] *RO4000 Series—High Frequency Circuit Materials*, Datasheet PUB# 92-004, Rogers Corp., Chandler, AZ, USA, 2018.

[45] *6 Series MSO Mixed Signal Oscilloscope Datasheet*, Datasheet 48W-61353-3, Tektronix, Beaverton, OR, USA, Aug. 2018.

[46] L. Marple, "Computing the discrete-time 'analytic' signal via FFT," *IEEE Trans. Signal Process.*, vol. 47, no. 9, pp. 2600–2603, Sep. 1999.

[47] F. R. Kschischang, "The Hilbert transform," Lecture Notes From the Edward S. Rogers Sr. Dept. Elect. Comput. Eng., Univ. Toronto, Toronto, ON, Canada, Mar. 2015. [Online]. Available: https://www.Commun.utoronto.ca/frank/notes/hilbert.pdf

[48] T. Zwick, W. Wiesbeck, J. Timmermann, and G. Adamiuk, *Ultra-Wideband RF System Engineering* (EuMA High Frequency Technologies Series), 1st ed. Cambridge, U.K.: Cambridge Univ. Press, 2013.

[49] (2022). *Hilbert: Discrete-Time Analtyical Signal Using Hilbert Transform*. Math-Works MATLAB Help Center. [Online]. Available: https://www.mathworks.com/help/signal/ref/hilbert.html

[50] P. Welch, "The use of fast Fourier transform for the estimation of power spectra: A method based on time averaging over short, modified periodograms," *IEEE Trans. Audio Electroacoust.*, vol. AU-15, no. 2, pp. 70–73, Dec. 1967.

[51] (2022). *pwelch: Welch's Power Spectral Density Estimate*. MathWorks MATLAB Help Center. [Online]. Available: https://www.mathworks.com/help/signal/ref/pwelch.html

[52] *Rubidium Frequency Standard Model FE-5680A Series: Operation and Maintenance Instructions*, Freq. Electron., Inc., Mitchel Field, NY, USA, Nov. 2002.

[53] *Coaxial 50W 10 dB Directional Coupler 0.5–6 GHz*, Datasheet RFBC5M06G10 Rev. 5.0, RF-Lambda, Jun. 2022.

[54] *Keysight Technologies Infiniivision 6000 X-Series Oscilloscope*, Datasheet 5991-4087EN, Keysight Technol., Santa Rosa, CA, USA, 2018.

[55] *Evaluating Oscilloscope Vertical Noise Characteristics*, Keysight Technol., Santa Rosa, CA, USA, Aug. 2019.

Aaron D. Pitcher (Graduate Student Member, IEEE) received the B.E. degree (Hons.) in electrical engineering and the M.A.Sc. degree in electrical and computer engineering from McMaster University, Hamilton, ON, Canada, in 2016 and 2019, respectively. His Ph.D. research is focused on developing characterization and calibration techniques for short-range ultrawideband (UWB) pulsed-radar systems for the deembedding of target signatures.

His research interests include the application of microwaves in security and personnel protection systems, imaging diagnostics, and space communication.

Mr. Pitcher currently holds the Doctoral Alexander Graham Bell Canada Graduate Scholarship from the Natural Science and Engineering Research Council (NSERC) of Canada awarded in 2020.

Charl W. Baard received the B.E. degree in electrical and electronic engineering and the Ph.D. degree from Stellenbosch University, Stellenbosch, South Africa, in 2009 and 2013, respectively.

His interests include RF component and system designs intended to use in high-performance microwave sensors.

Natalia K. Nikolova (Fellow, IEEE) received the Dipl.Eng. degree in radio electronics from the Technical University of Varna, Varna, Bulgaria, in 1989, and the Ph.D. degree from The University of Electro-Communications, Tokyo, Japan, in 1997.

From 1998 to 1999, she held a Post-Doctoral Fellowship of the Natural Sciences and Engineering Research Council of Canada (NSERC). In 1999, she joined the Department of Electrical and Computer Engineering, McMaster University, Hamilton, ON, Canada, where she is currently a Professor. Her research interests include inverse scattering, microwave and millimeter-wave imaging, and computer-aided analysis and design of high-frequency structures and antennas.

Prof. Nikolova is also a fellow of the Canadian Academy of Engineering and the Engineering Institute of Canada. She has served as an IEEE Distinguished Microwave Lecturer from 2010 to 2013.